International Journal of
Automotive Manufacturing and Materials（IJAMM）

Scilight

Article

The Influence of Initial Billet Design on the Ring Rolling Deformation and Residual Stress Distribution of GH3044 Alloy

Xiaoluo Gu [1,*], Qianzhi Peng [1], and Hongxing Lu [2,*]

[1] AECC South Industry Company Limited, Zhuzhou 412000, China
[2] Department of Mechanical and Energy Engineering, Southern University of Science and Technology, Shenzhen 518055, China
* Correspondence: xiaoluo_gu@126.com (X.G.); luhx@sustech.edu.cn (H.L.)
Received: 3 June 2025; Revised: 25 June 2025; Accepted: 1 July 2025; Published: 15 August 2025

Abstract: Gleeble thermal simulation tests established the elastoplastic constitutive equation of GH3044. Using this constitutive relationship, the influence of three initial billet designs on ring rolling deformation and post-forging residual stress was simulated in the Forge finite element software. The results indicate that when there is a significant difference between the thickness and height dimensions of the ring, the primary rolling direction in the initial billet design should avoid aligning with either the excessively tall or excessively thick direction of the ring. After the ring rolling process is completed and cooled, the edges and corners of the ring's end face experience compressive stress, while the core is subjected to tensile stress. This distribution aligns with the strain field distribution pattern of the ring.

Keywords: radial-axial rolling; GH3044; temperature field; strain field; residual stress

1. Introduction

GH3044 is a Ni-Cr-based solid-solution strengthened wrought superalloy with high strength and ductility, excellent oxidation resistance, stamping, and welding properties. It possesses moderate creep and stress rupture strength below 900 °C and good cold-forming and welding capabilities. This alloy is particularly suitable for manufacturing sheet metal components of aero-engine main combustion chambers, afterburners, and other high-temperature parts designed for long-term service below 900 °C and the high-temperature structural components in automobile turbochargers [1–4].

Radial-axial rolling is currently the mainstream process for forming ring forgings. Reported research on the radial-axial ring rolling processes of nickel-based superalloys focuses on microstructural evolution, mechanical properties, and processing techniques, highlighting advancements in material performance for gas turbine applications [5–7]. These studies emphasize the importance of understanding how different processing methods and microstructural characteristics influence the mechanical behavior of these alloys. The study on ring-rolling processes highlighted the importance of optimizing geometrical constraints and alloy design to improve manufacturability and reduce processing time significantly [8]. The numerical modeling of rotary forging processes provided insights into the effects of processing parameters on microstructural behavior, enhancing the understanding of deformation mechanisms [9]. In the design of radial-axial ring rolling processes, the initial billet design is a critical step affecting the forming quality of the ring. An unreasonable initial billet design not only easily leads to dimensional defects such as fishtails, dishing, and warping in the ring but also, due to its influence on the strain field and temperature distribution during ring rolling, tends to cause microstructural defects.

This study employed Gleeble thermal simulation tests to establish the thermo-elastoplastic constitutive equation of GH3044. The ring rolling processes with different initial billet designs were simulated using

Forge software (V1.1, Transvalor, Sophia Antipolis, France), and the influence of various initial billet designs on ring rolling deformation and post-forging residual stress distribution was analyzed. The research aims to provide theoretical guidance for the design of rolling process parameters for GH3044 alloy ring forgings.

2. Materials and Methods

Figure 1 shows the profile and dimensions of the GH3044 ring studied in this paper.

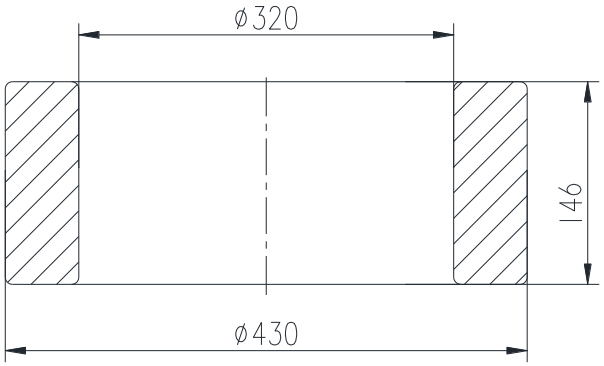

Figure 1. Dimensions of GH3044 Alloy Ring (unit: mm).

The experimental approach of this study involves constructing the constitutive equation of GH3044 alloy through Gleeble hot compression tests and JMatPro software (V7.0.0, Sente Software Ltd., Guildford, UK). This equation is then applied in Forge software to analyze the rolling deformation under three billet preparation schemes. Finally, the distribution of residual stresses in the ring during and after the cooling process is examined.

First, the thermo-elastoplastic constitutive equation of GH3044 was established using Gleeble tests and JMatPro software. The Gleeble thermal simulation tests were conducted on a Gleeble 3800 thermal/mechanical simulator. The physical specimen and dimensions of the hot compression test are shown in Figure 2.

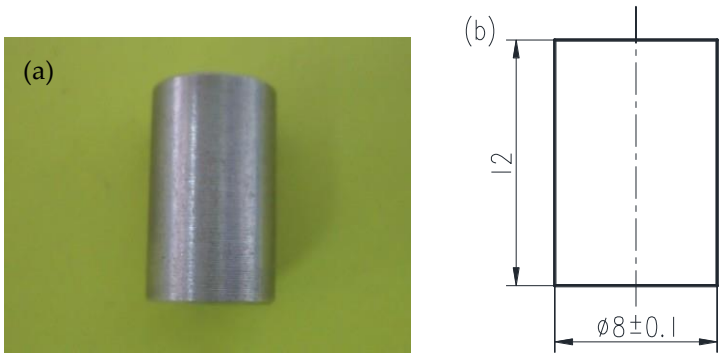

Figure 2. Gleeble specimen and dimensions: (**a**) Physical Gleeble specimen; (**b**) Dimensions of Gleeble specimen (unit: mm).

The strain rates for the hot compression tests were set at: 0.1 s^{-1}, 1 s^{-1}, 10 s^{-1}, and 50 s^{-1}, while the deformation temperatures were set at 1020 °C, 1070 °C, 1120 °C, and 1180 °C, respectively. Figure 3 shows the flow curves of GH3044 alloy under the specified test parameters.

By appropriately processing the flow stress data, the high-temperature constitutive equation based on the Hansel-Spittel model can be derived, as shown in Equation (1):

$$\sigma = 4235.12 \cdot e^{-0.0031T} \cdot \varepsilon^{-0.25} \cdot \dot{\varepsilon}^{0.16} \cdot e^{-\frac{0.09}{\varepsilon}} \quad (1)$$

The variation curves of elastic modulus and Poisson's ratio for GH3044 alloy with temperature are shown in Figure 4.

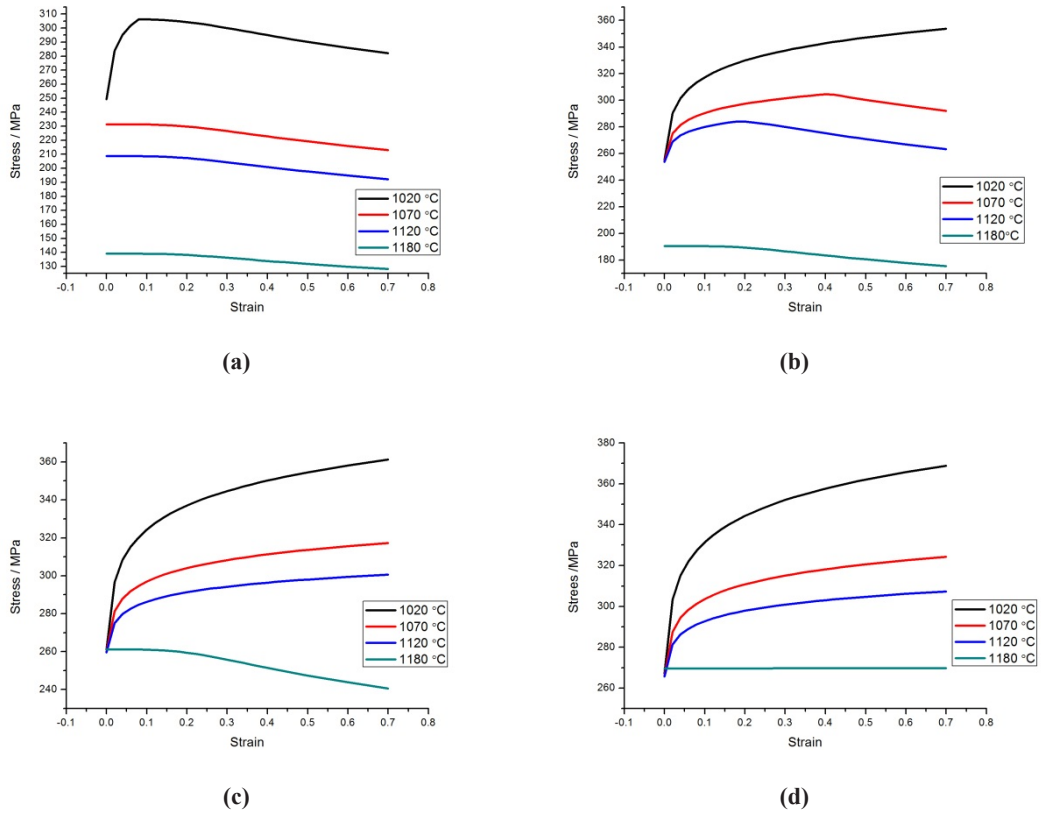

Figure 3. Flow curves of GH3044 under different temperatures and strain rates: (**a**) $\dot{\varepsilon} = 0.1\ s^{-1}$; (**b**) $\dot{\varepsilon} = 1\ s^{-1}$; (**c**) $\dot{\varepsilon} = 10\ s^{-1}$; (**d**) $\dot{\varepsilon} = 50\ s^{-1}$.

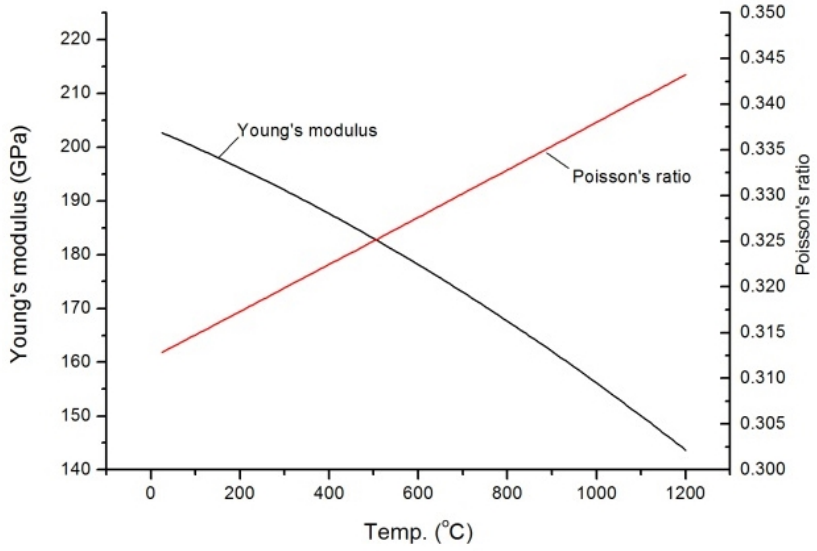

Figure 4. Variation curves of elastic modulus and Poisson's ratio with temperature.

In addition to the constitutive relationship, other parameters used for the simulation include: a billet heating temperature of 1160 °C, die preheating temperature of 250 °C, ambient temperature of 20 °C, friction coefficient of 0.8, thermal radiation coefficient of 0.58, and thermal conductivity of 6.7. The rotational speed of the main roller is 40 r/min.

Using the data, the rolling processes of three initial billet schemes were simulated in the Forge finite

element software. Figure 4 shows the shape and dimensions of the GH3044 alloy ring studied in this paper.

Figure 5 presents the three designed initial billet schemes. Among them, Scheme I is based on the Vieregge relationship [10], specifically:

$$\frac{\Delta b}{\Delta h} = \frac{h}{b} \tag{2}$$

Where Δb and Δh represent the rolling reductions in the thickness and height directions of the ring, respectively, while h and b denote the height and thickness of the ring, option II allocates the entire rolling reduction to the axial direction of the ring. At the same time, Option III assigns the whole of the rolling reduction to the radial direction of the ring. All three options share the same inner diameter dimension of Φ200 mm.

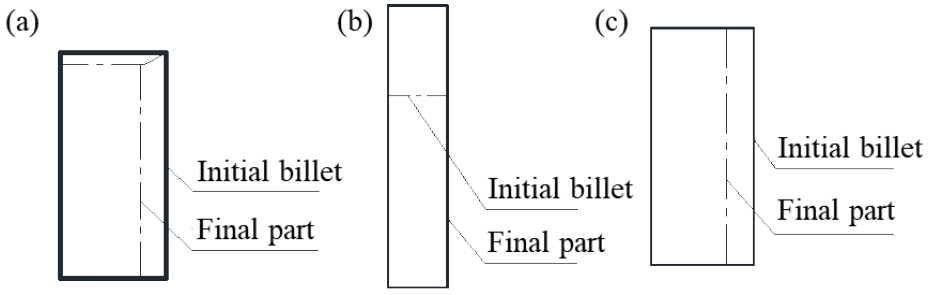

Figure 5. Initial billet design schemes: (**a**) Scheme I; (**b**) Scheme II; (**c**) Scheme III.

3. Results and Discussion

3.1. The Influence of Initial Billet Design on Strain Field and Temperature Field

Figure 6 shows the equivalent strain diagrams of the three schemes after rolling completion. In Figure 6a, it can be observed that in Scheme I, the regions with high strain are mainly concentrated at the corner edges of the upper and lower end faces, while the strain in the central area of the ring cross-section is relatively small. The maximum strain value is 4.64, the minimum is 0.4, and the range is 4.24. Figure 6b displays the strain field distribution of Scheme II. This figure shows that the areas with the highest strain in the forging cross-section are primarily located at the upper and lower end faces, particularly at the outer circular corner edges. The maximum strain value here is 24.96, while the regions with lower strain are situated in the central part of the ring cross-section, with a minimum strain value of 0.34, resulting in a range of 24.62. Figure 6c illustrates the strain field distribution of Scheme III. Like the previous two schemes, the highest strain occurs at the outer circular corner edges of the upper and lower end faces, with a maximum strain value of 3.29. The lowest strain is found in the central region of the ring cross-section, with a minimum value of 0.46, yielding a range of 2.83. By comparing the strain field distributions and magnitudes of the three schemes, it is evident that Scheme III exhibits a higher minimum strain than Schemes I and II, and the area of low-strain regions in the forging cross-section is smaller than in Schemes I and II. Therefore, Scheme III's deformation is more uniform than Schemes I and II.

The regions with the highest strain are primarily located at the outer circular corner edges of the upper and lower end faces. This is mainly because rolling involves small and continuous deformation, making it difficult for the deformation to fully penetrate the entire forging cross-section as the billet passes through the rollers with a small feeding amount. Small protrusions form at the end faces when the billet passes through the rolling groove. As the ring continuously passes through the rolling groove, the corner edges of the upper and lower end faces undergo repeated deformation, resulting in significantly large deformation in these areas. The specific mechanism is illustrated in Figure 7. Scheme II exhibits the highest strain range of 24.62 among the three schemes. This is primarily because the deformation mainly occurs in the axial direction. In contrast, the axial height is significant, making it difficult for the deformation zone to penetrate the entire cross-section fully. As a result, deformation concentrates predominantly on the surface while the core region undergoes minimal deformation.

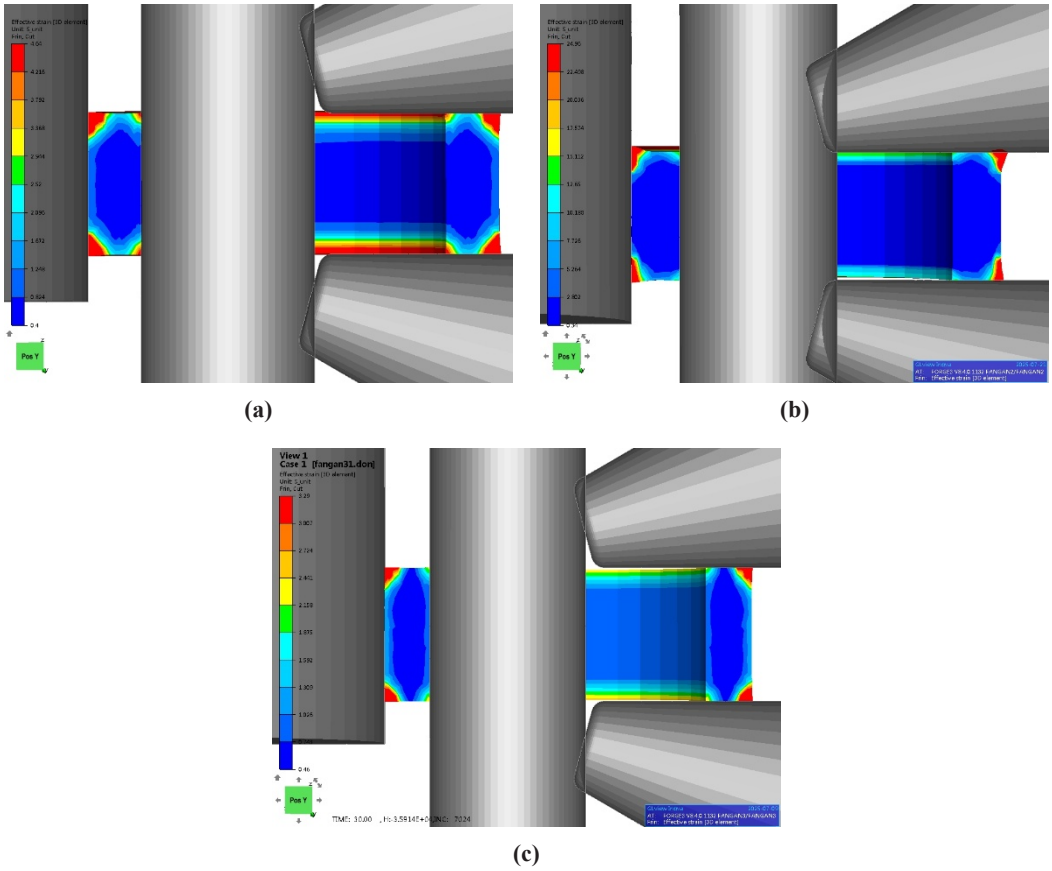

Figure 6. Equivalent strain distribution of the three schemes upon completion of rolling: (**a**) Scheme I; (**b**) Scheme II; (**c**) Scheme III.

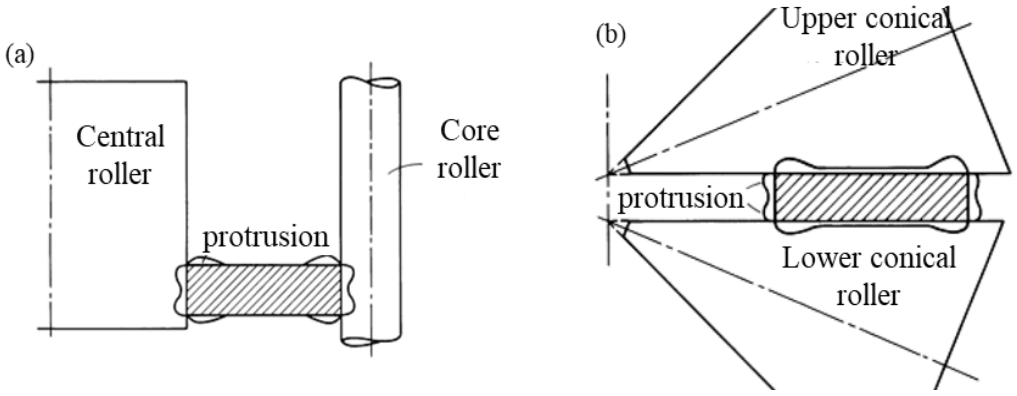

Figure 7. Formation of corner protrusions during the rolling process as the billet passes through the groove: (**a**) Formation of protrusions when the billet passes through the central roller/core roller groove; (**b**) Formation of protrusions when the billet passes through the upper/lower conical roller groove.

Figure 8 shows the temperature field distribution after rolling for the three schemes. As can be seen from the figure, Schemes I and III exhibit similar temperature distributions, with higher temperatures in the core and lower temperatures on the surface. The maximum temperature is approximately 1147 °C, lower than the initial rolling temperature of 1160 °C. This is primarily because the billet is in contact with the rolls and the atmosphere during rolling, leading to heat dissipation through conduction, radiation, and convection. As a result, the surface temperature is significantly lower than the core temperature. Additionally, due to the small deformation amount and relatively slow deformation speed, the heat generated by deformation is insufficient

to compensate for the heat loss, causing the maximum temperature after rolling to be lower than the initial forging temperature. However, Scheme II's temperature distribution differs significantly from Schemes I and III, with high-temperature zones near the upper and lower end faces. The maximum temperature reaches 1174 °C, exceeding the initial forging temperature. This is mainly because the regions near the upper and lower end faces are large deformation zones, and the rolling speed of the conical rolls is significantly higher than in Schemes I and III. Consequently, the strain rate is higher, leading to greater power generation from deformation heat than in Schemes I and III. The heat generated by deformation exceeds the heat loss through contact and radiation, resulting in localized temperature increases in the billet. Therefore, based on the simulation results, if the primary rolling direction is aligned with the billet's excessively tall or thick dimension, the roll speed in that direction must be increased within a given rolling time. This leads to a significant rise in power output in that direction. Moreover, since deformation is concentrated on the surface under such conditions, the forging cannot fully penetrate, and the ring cannot grow properly. Only a small portion of the roll's output work is converted into deformation energy for the ring. In contrast, the remaining energy is dissipated as heat, causing a severe temperature to rise in the surface metal. Under these circumstances, the elevated temperature of the surface metal reduces its deformation resistance, making it more prone to deformation. If rolling continues, defects such as overheating, burning, folding, or even cracking may occur in the billet. Additionally, temperatures exceeding the initial forging temperature can result in an unqualified microstructure of the forged part. Furthermore, according to the power expression:

$$W = F \times V \tag{3}$$

When the deformation resistance is high, the power output of the rolls will increase. Therefore, this situation should be avoided during the initial billet design stage, particularly for difficult-to-deform metals such as superalloys.

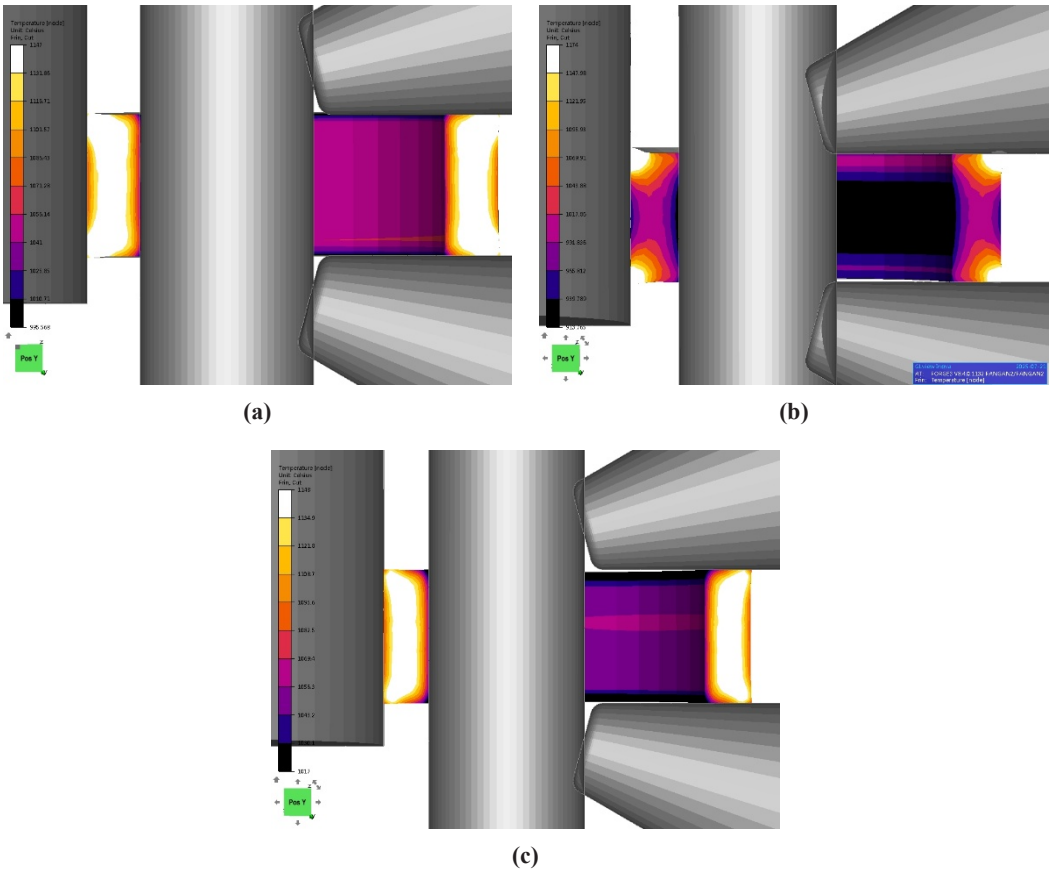

Figure 8. Temperature field distribution after rolling: (**a**) Scheme I; (**b**) Scheme II; (**c**) Scheme III.

Therefore, based on the analysis of strain field and temperature field distributions, the following conclusions can be drawn: (1) Scheme III demonstrates superior deformation uniformity compared to Schemes I and II; (2) The temperature field distributions of Schemes I and III exhibit better uniformity than Scheme II; (3) When there is significant dimensional disparity between ring thickness and height, the primary rolling direction should not be aligned with the excessively tall or thick dimension during initial billet design to prevent incomplete penetration during rolling; (4) For rings with substantial wall thickness, large-diameter mandrels and high feed rates should be employed during rolling to ensure process parameters meet forging penetration requirements, thereby preventing surface-concentrated deformation that causes temperature rise and avoiding rolling defects [11,12].

Based on the previous analysis, Scheme III was selected as the initial billet preparation method, and rolling tests were conducted. The physical rolling results are shown in Figure 9, where no significant defects such as fishtails or folds are observed on the ring's end faces. Figure 10 presents the metallographic structures of the ring's end face and core section. The microstructures show minimal difference between these regions, with grain sizes consistently ranging between Grades 4 and 6.

Figure 9. Physical specimen of GH3044 alloy ring.

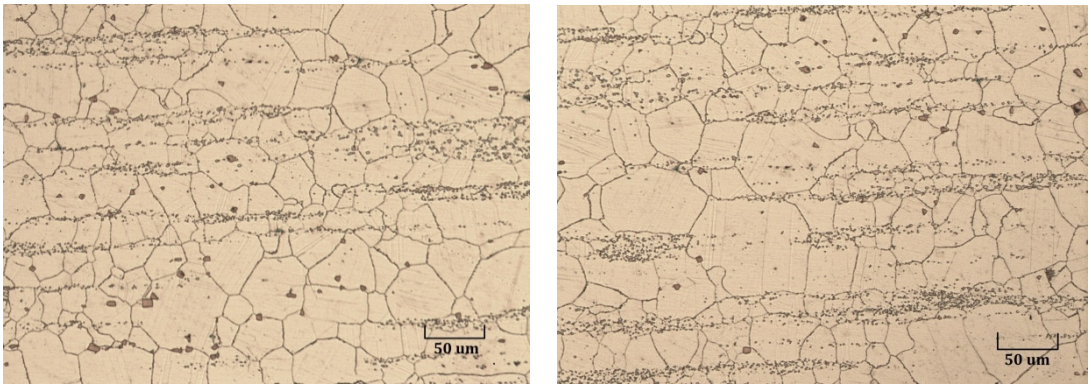

(a) **(b)**

Figure 10. Metallographic structure of the ring's end face and core section: (**a**) End face; (**b**) Core section.

3.2. Variation of Residual Stress during the Forging Cooling Process

Based on the previous analysis, the deformation uniformity of Scheme III is superior to that of Schemes I and II. Therefore, Scheme III is selected as the research subject to analyze the variation patterns of residual stress during the post-forging cooling process.

Figure 11 shows the distribution of the equivalent stress field at the end of rolling and when cooling begins after roller unloading. As can be seen from the figure, when the rollers are not unloaded, the location

of maximum stress is at the roller clamping area, with a peak stress value of 151.765 MPa. After roller unloading, the stress concentration zone formed by roller clamping disappears, and the maximum stress region shifts to the edge corners of the end face. Internal stresses in the forging become non-uniform, with a Maximum of 37.9 MPa and a minimum of 5.38 MPa. These residual stresses are caused by non-uniform deformation during the process.

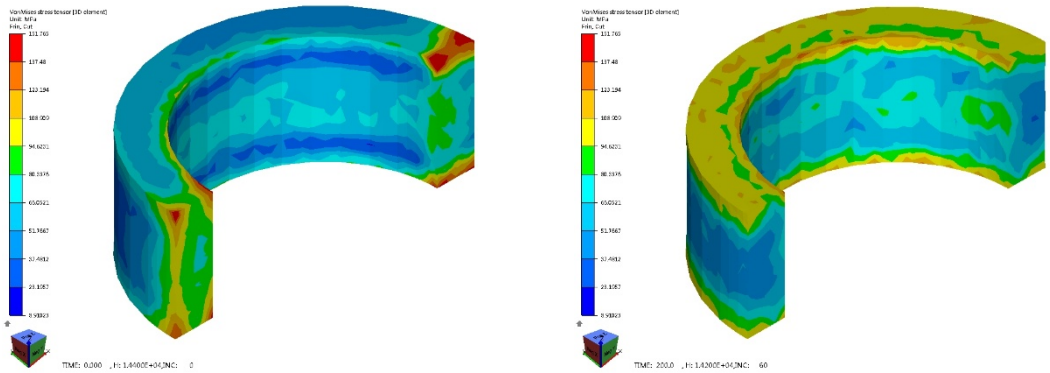

(a) **(b)**

Figure 11. Distribution of equivalent stress before and after roller unloading: (**a**) Equivalent stress distribution before roller unloading, (**b**) Equivalent stress distribution after roller unloading.

Figure 12 shows the temperature and equivalent stress variation curves of three points inside the ring over time. From the graph, as time goes on, the temperature decreases at 3 points. And the equivalent force gradually increases with time and finally tends to stabilize. The variation law of equivalent stress is mainly due to: (1) as the surface layer of the ring cools, the uneven shrinkage of the surface metal and the core metal will lead to the generation of thermal stress; (2) as the temperature decreases, the elastic modulus gradually increases, and the stress generated per unit strain will increase. Therefore, as the temperature gradually decreases, the level of equivalent stress significantly increases.

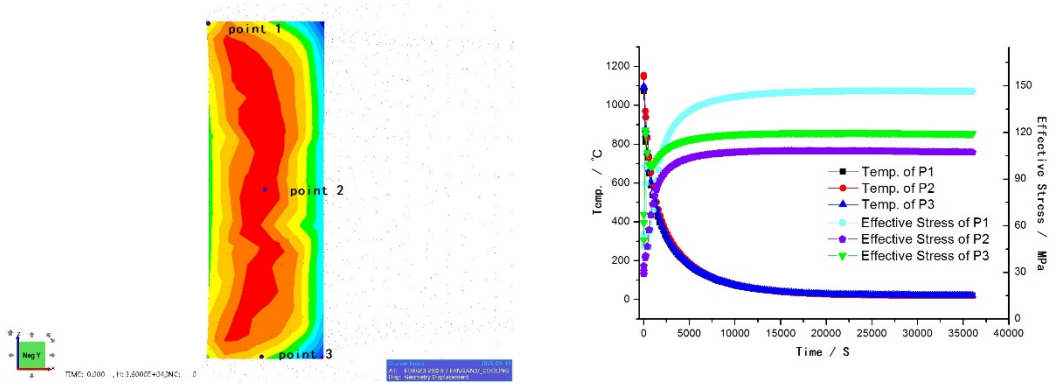

(a) **(b)**

Figure 12. The variation curves of temperature and equivalent stress at three points inside the ring over time: (**a**) taking the point positions; (**b**) Temperature and equivalent stress variation curves over time.

Figure 13 shows the distribution of principal stresses inside the ring when cooling begins after unloading the rolling mill. It can be seen from the figure that there is a triaxial compressive stress state at the corners of the ring end face. At the same time, the core is subjected to a triaxial compressive stress state, and the direction of maximum principal stress is along the circumference of the ring.

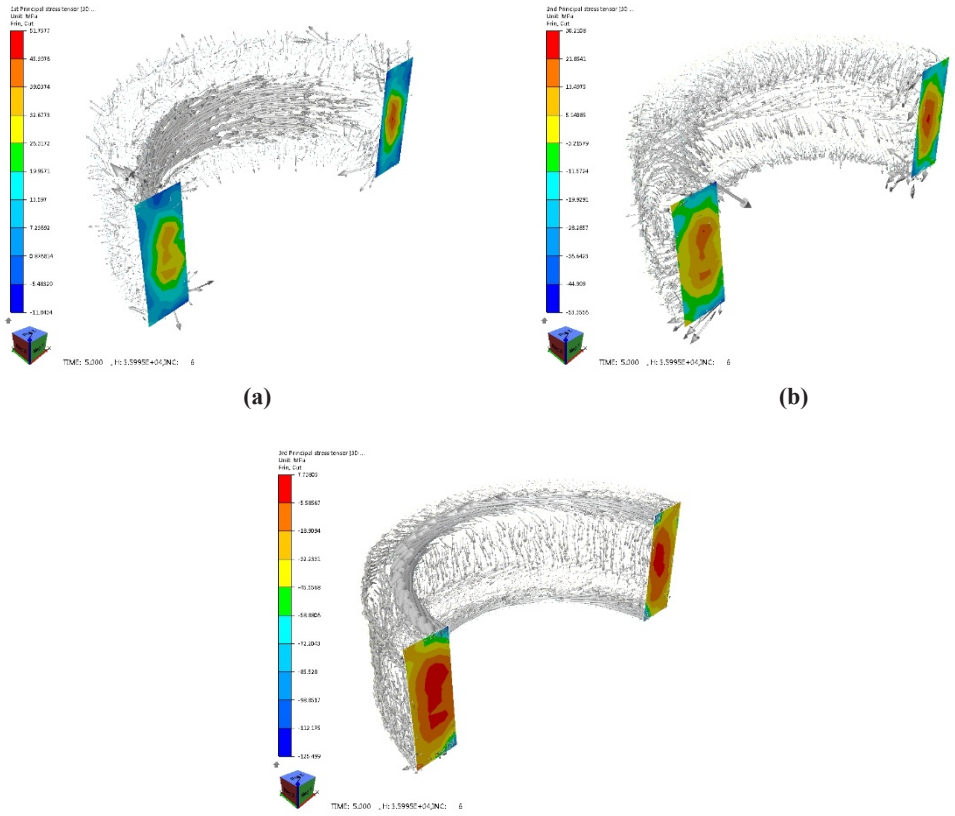

Figure 13. The distribution of principal stresses inside the ring at the beginning of cooling: (**a**) the first principal stress; (**b**) the Second principal stress; (**c**) the Third principal stress.

Figure 14 shows the ring's temperature field and three-dimensional principal stress distribution when cooled to 240 s. From the figure, there has been a significant change in the distribution of principal stress at this time, with the maximum areas of principal stress gradually divided into two regions. This is mainly due to the enhanced cooling shrinkage of the upper and lower end faces, causing the central tensile stress region to move progressively towards both ends. The positions of point 1, point 2, and point 3 (as shown in Figure 12) are affected by the superposition of thermal stress and uneven deformation stress during rolling, resulting in a decrease in all three principal stresses and a reduction in equivalent stress.

Figure 15 shows the temperature field and distribution of the principal stress field of the forging after cooling for 3600 s. From Figure 15a, at this point, the surface temperature of the forging has decreased to 271 °C, the core temperature is 255 °C, and the surface temperature of the forging tends to be uniform. Therefore, the surface of the forging shrinks uniformly, causing a change in the direction of the first principal stress, from the original distribution along the circumference to perpendicular to the normal direction of the forging surface. At the same time, the center of the ring is in a state of triaxial tensile stress, with the second principal stress direction along the circumferential direction of the ring and the third principal stress direction along the axial direction of the ring.

Figure 16 shows the distribution of the temperature field and the equivalent stress field of the forging after 10 h of cooling. It can be seen from the figure that the temperature of the forging after 10 h of cooling is consistent with the ambient temperature (ambient temperature 20 °C), with a maximum temperature of 20.5 °C and a minimum temperature of 20.4 °C. Figure 16b shows the equivalent stress distribution. It can be seen from this figure that when the forging is uniformly cooled to room temperature, there is still significant residual stress inside the forging, and the maximum equivalent stress is located at the inner circle of the upper and lower end faces.

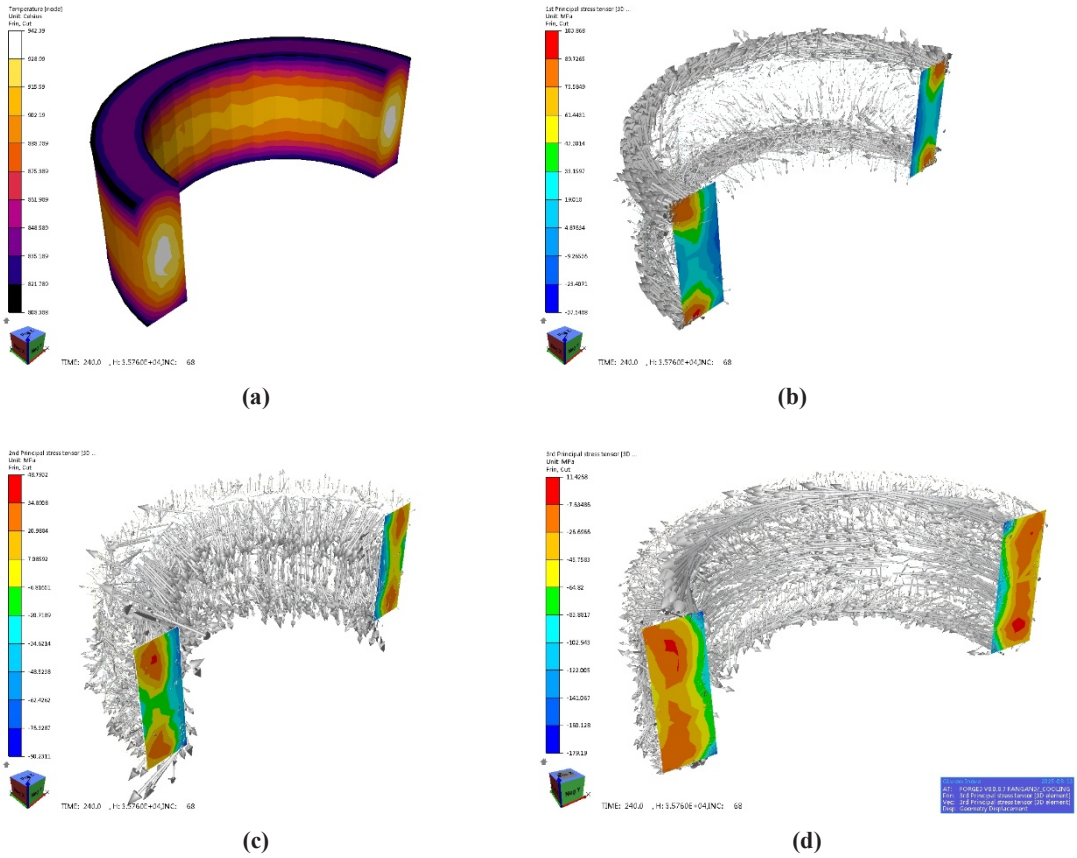

Figure 14. Temperature field and principal stress distribution of the ring after 240 s of cooling: (**a**) Temperature field distribution; (**b**) First principal stress; (**c**) Second principal stress; (**d**) Third principal stress.

Figure 17 shows the distribution and direction of the triaxial principal stress inside the forging after cooling to room temperature. It can be seen from the figure that the interior of the ring is in a triaxial tensile stress state, with the first principal stress distributed along the circumference. At the same time, it can be observed that the corners of the ring's upper and lower end faces are under varying degrees of compression. Figure 17c shows that the maximum compressive stress at the corners reaches 364.496 MPa and is distributed along the ring's circumference.

The formation of this stress state is mainly related to the strain field distribution of the forging. As analyzed earlier, after rolling is completed, the deformation at the inner and outer corners of the ring's upper and lower end faces is significant, mainly elongation along the circumferential direction. In contrast, the deformation at the center of the ring is small. Therefore, it causes the metal at the corners of the upper and lower end faces of the ring to pull the metal at the center and elongate it in the circumferential direction, increasing the overall size of the ring and a stress state of compression at the corners of the end faces and tension at the center. Therefore, although the stress state changes during the cooling process after forging, when the overall temperature of the forging is uniform and there is no thermal stress, the distribution of residual stress conforms to the strain field distribution law of the forging. Suppose the influence of heat treatment on residual stress distribution is not considered. In that case, it can be predicted based on the distribution of residual stress after forging that when the surface material of the ring is removed by subsequent machining, the ring will undergo shrinkage or deformation.

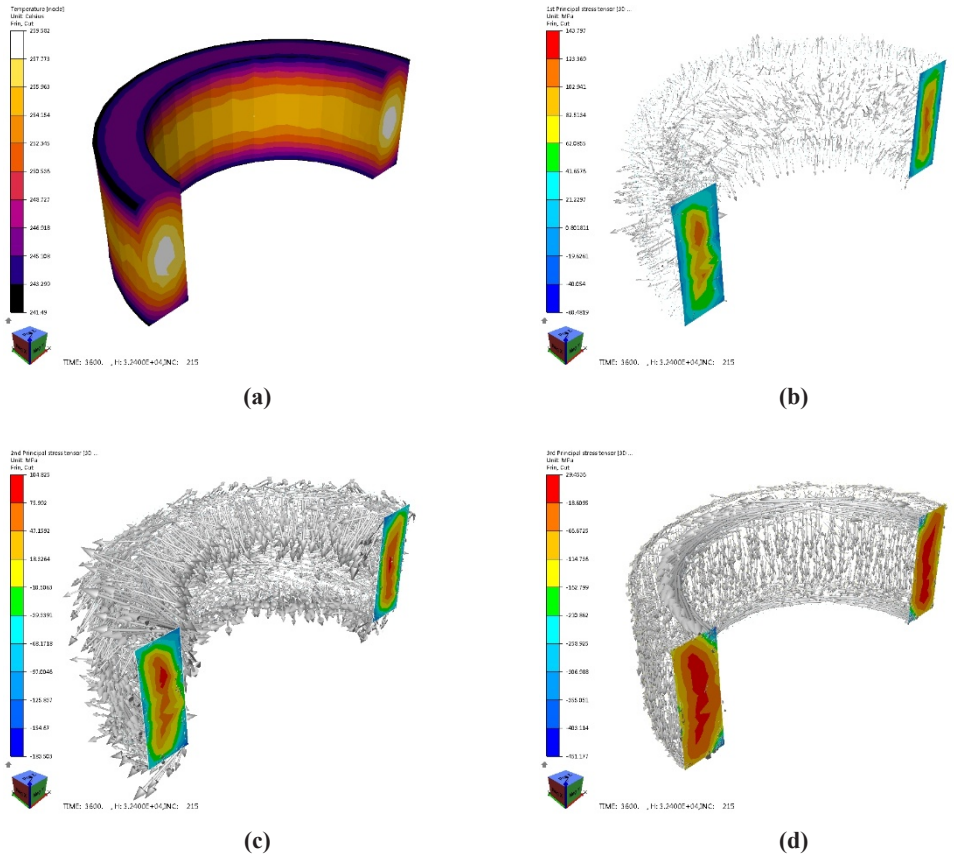

(a) **(b)** **(c)** **(d)**

Figure 15. Temperature field and principal stress distribution of the ring after 3600 s cooling: (**a**) Temperature field distribution; (**b**) First principal stress; (**c**) Second principal stress; (**d**) Third principal stress.

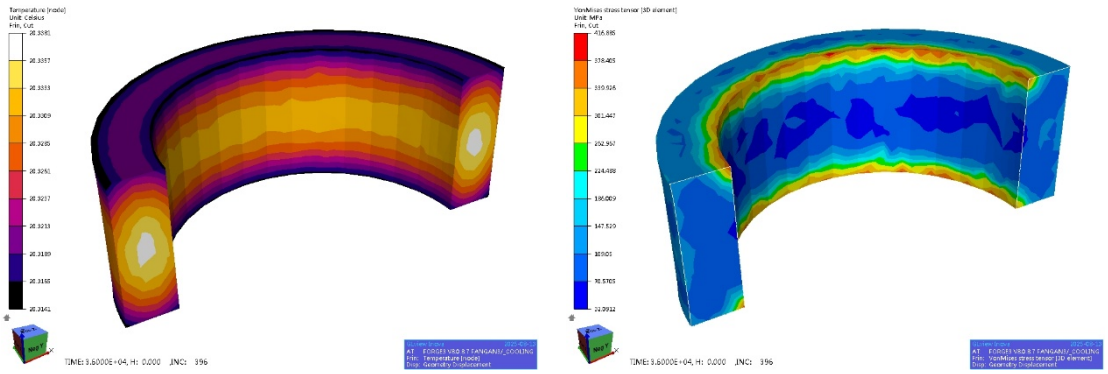

(a) **(b)**

Figure 16. Temperature field and equivalent stress field distribution of forgings after 10 h of cooling: (**a**) Temperature field; (**b**) Equivalent stress field.

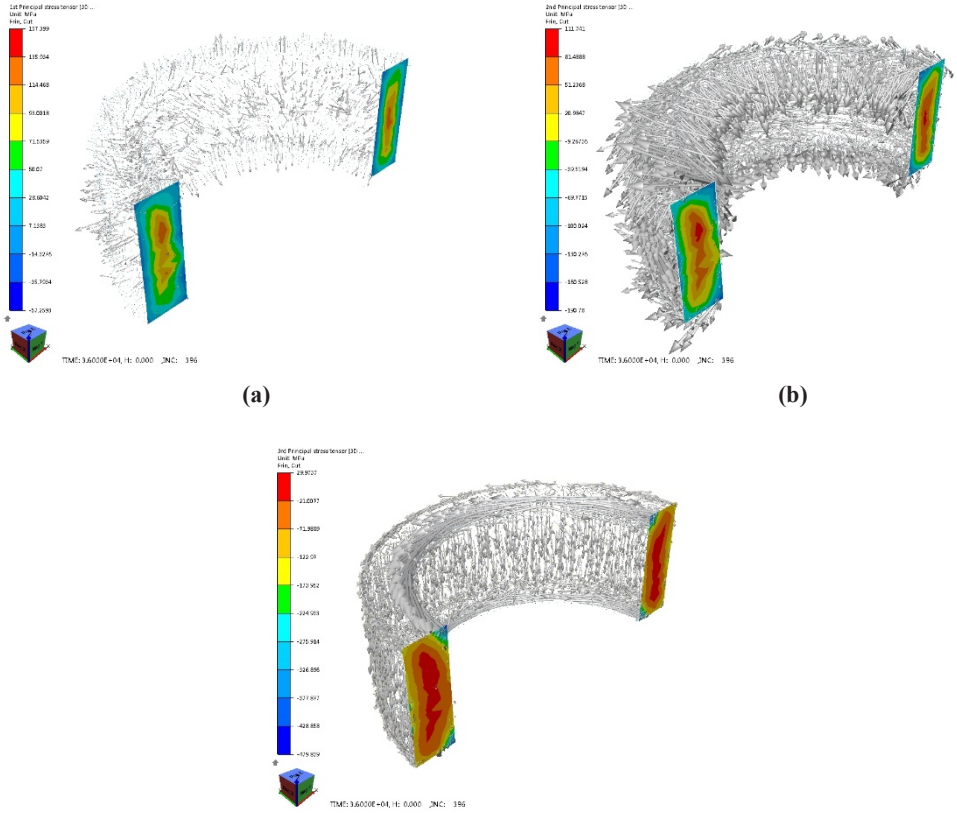

Figure 17. Distribution of principal stresses inside the forging after 10 h of cooling: (**a**) First principal stress; (**b**) Second principal stress; (**c**) Third principal stress.

4. Conclusions

The influence of initial billet design on the ring rolling deformation of GH3044 alloy and residual stress distribution after forging was analyzed using Forge finite element software. The following conclusions were drawn:

(1) The uniformity of strain field distribution and temperature field distribution in Scheme III is superior to that of Schemes I and II. Through actual trial production, Scheme III can obtain qualified forgings.

(2) When there is a significant difference between the thickness and height dimensions of the ring, the main rolling direction should not be arranged in the direction where the ring is too high or too thick during the initial billet design.

(3) After the cooling process of the ring rolling is completed, additional compressive stress is applied to the corners of the ring end face, and additional tensile stress is applied to the center, consistent with the ring's strain field distribution.

Author Contributions: X.G.: conceptualization, methodology, writing—original draft preparation; Q.P.: investigation, data curation, visualization; H.L.: methodology, writing—reviewing and editing. All authors have read and agreed to the published version of the manuscript.

Funding: This research received no external funding.

Institutional Review Board Statement: Not applicable.

Informed Consent Statement: Not applicable.

Data Availability: Statement: Not applicable.

Conflicts of Interest: The authors declare no conflict of interest.

References

1. Wang, L.; Dong, J.; Tian, Y.; Xie, X. Research on Macroscopic Segregation Behavior and Element Segregation Law during Solidification Process of GH3044 Alloy. *Rare Met. Mater. Sci. Eng.* **2019**, *35*, 1408–1411.
2. Zhang, S.; Yu, H.; Li, Y. Research on High Temperature and Low Cycle Fatigue Performance of GH3044. *J. Aeronaut. Mater.* **2013**, *33*, 100–103.
3. Yin, C.; Dai, C.; Li, W.; Yu, G.; Deng, J. Analysis and Countermeasure of Cracking of the Supercharger Inlet Pipe of a Diesel Engine. *Int. J. Automot. Manuf. Mater.* **2025**, *4*, 6.
4. Miao, X.; Xu, B.; Deng, J.; Li, L. Key Technologies to 50% Brake Thermal Efficiency for Gasoline Engine of Passenger Car. *Int. J. Automot. Manuf. Mater.* **2025**, *4*, 1.
5. Berti, G. A.; Quagliato, L.; Monti, M. Set-up of radial-axial ring-rolling process: Process worksheet and ring geometry expansion prediction. *Int. J. Mech. Sci.* **2015**, *99*, 58–71.
6. Tang, X.; Wang, B.; Zhang, H.; Fu, X.; Ji, H. Study on the microstructure evolution during radial-axial ring rolling of IN718 using a unified internal state variable material model. *Int. J. Mech. Sci.* **2017**, *128*, 235–252.
7. Zhu, X.; Liu, D.; Yang, Y.; Hu, Y.; Zheng, Y. Optimization on cooperative feed strategy for radial-axial ring rolling process of Inco718 alloy by RSM and FEM. *Chin. J. Aeronaut.* **2016**, *29*, 831–842.
8. Adziman, F.; Takai, R.; Tang, Y. T.; Ishikawa, S.; Barba, D.; Alabort, E.; Nemeth, A.; Kanno, N.; Reed, R. On Optimising Ring-Rolling Manufacturability of C&W Nickel Superalloys for Aero-engine Turbine Disc. *Superalloys* **2020**, *2020*, 408–420.
9. Loyda, A.; Reyes, L. A.; Hernández-Muñoz, G. M.; García-Castillo, F. A.; Zambrano-Robledo, P. Influence of the incremental deformation during rotary forging on the microstructure behaviour of a nickel-based superalloy. *Int. J. Adv. Manuf. Technol.* **2018**, *97*, 2383–2396.
10. *ASM Metal Handbook*; Volume 14: Forming and Forging; ASM International: Almere, The Netherlands, 1996.
11. Lin, H. *Ring Rolling Theory and Technology*; Wuhan University of Science and Technology Press: Wuhan, China, 2000.
12. Eruc, E.; Shivpuri, R. A summary of ring rolling technology—II: Recent trends in process, modeling, simulation, planning, and control. *Int. J. Mach. Tools Manufact.* **1992**, *32*, 399–413.